Edge-Enhanced Image Reconstruction Using (TV) Total Variation and Bregman Refinement

Shantanu H. Joshi[1], Antonio Marquina[2,3], Stanley J. Osher[3], Ivo Dinov[1],
John D. Van Horn[1], and Arthur W. Toga[1]

[1] Laboratory of Neuroimaging, University of California, Los Angeles, CA 90095, USA
[2] Departamento de Matematica Aplicada, Universidad de Valencia,
C/ Dr Moliner, 50, 46100 Burjassot, Spain
[3] Department of Mathematics, University of California, Los Angeles, CA 90095, USA

Abstract. We propose a novel image resolution enhancement method for multidimensional images based on a variational approach. Given an appropriate down-sampling operator, the reconstruction problem is posed using a deconvolution model under the assumption of Gaussian noise. In order to preserve edges in the image, we regularize the optimization problem by the norm of the total variation of the image. Additionally, we propose a new edge-preserving operator that emphasizes and even enhances edges during the up-sampling and decimation of the image. Furthermore, we also propose the use of the Bregman iterative refinement procedure for the recovery of higher order information from the image. This is coarse to fine approach for recovering finer scales in the image first, followed by the noise. This method is demonstrated on a variety of low-resolution, natural images as well as 3D anisotropic brain MRI images. The edge enhanced reconstruction is shown to yield significant improvement in resolution, especially preserving important edges containing anatomical information.

Keywords: Edge-preserving operators, total variation regularization, deconvolution, Gaussian blur, Bregman iteration, up/down sampling.

1 Introduction

With the recent advances in low-cost imaging solutions and increasing storage capacities, there is an increased demand for better image quality in a wide variety of applications involving both image and video processing. Often times, owing to sensor shortcomings, low-power requirements, or environmental limitations, one is only able to acquire a low-resolution observation of the scene. The low-resolution data can exist in the form of still images, a sequence of image frames devoid of inter-frame motion, a single video sequence, or a collection of video sequences. Furthermore the observations can be corrupted by motion-induced artifacts either in the case of still images or videos. The collective approach that tackles the problem of reconstructing a high-resolution image from one or more of the above low-resolution observations is termed as super-resolution. There are several prominent approaches to this problem, all of them largely employing various cues such as sub-pixel shifts between successive frames, the camera blur, defocus, and zoom, etc. These approaches can be divided into two types, ones that use motion information between successive frames (e.g., video super-resolution), and

X.-C. Tai et al. (Eds.): SSVM 2009, LNCS 5567, pp. 389–400, 2009.

the others that use a motion-free approach. Most of these approaches usually expect multiple low-resolution observations as input. Super-resolution image reconstruction can be mathematically modeled as a nonlinear process consisting of a convolution operator acting on the image, followed by a down sampling operation and the mixing of additive noise. Most of the earlier research work in this area has been developed in the frequency domain approach using (discrete) Fourier transform and wavelet-transform based methods. For e.g. the approach of Tsai and Huang [13] first outlined the idea of super-resolution in their seminal paper. Peleg *et al.* [8] used the iterative back projection scheme to achieve image reconstruction. Yet another approach [12] uses projections on convex sets (POCS) of images to restrict the solution domain for reconstruction. A hybrid approach by Elad and Feuer [5] combines the POCS and the maximum likelihood approaches for both motion-based and motion-free super-resolution. A very different set of methods use the learning-based approach for super-resolution. The general idea here is to learn a set of image features from exemplar images and use them for the reconstruction of a high-resolution image. Capel and Zisserman [2] use PCA on face image databases to learn the image model and use it to reconstruct images from multiple views. Freeman *et al.* [6] learn a feature set of image patches that encode the relationships among different spatial frequencies from a large training set and use it as prior information for reconstructing higher frequencies for resolution enhancement. The reader is referred to an excellent monograph by Chaudhari and Joshi [4] for a comprehensive bibliography and references in the field. Along with a wide range of applications of super-resolution methods in tasks such as satellite image processing, surveillance, computer vision, and even video processing, there has been a considerable effort by researchers trying to apply these methods to medical imaging. In particular, MRI acquisitions usually have a low-resolution in the inter-slice direction, and it is of considerable interest to “fill-in” the intermediate slices. Carmi *et al.* [3] use sub-pixel shifted MR (Magnetic Resonance) images for high resolution reconstruction. Greenspan *et al.* [7] combine several low resolution images in the slice-select direction to achieve SR reconstruction. Kornprobst *et al.* [9] also achieve higher resolution in the slice-select direction for fMRI sequences.

While super-resolution methods attempt to exploit the information redundancy in several low-resolution observations of images, at times, only a single low-resolution instance of the image is available. This is sometimes the case in MRI images, where due to economic or health reasons, a patient is scanned only once over a period of time, or the time elapsed between successive scans may be too large to preserve any temporal coherence to take advantage of. Based on this assumption, we will focus mainly on the problem of single frame high resolution reconstruction of images. Our approach will be based upon a variational model that uses the TV norm [11] as a regularizing functional. Recently, Marquina *et al.* [14] have proposed a new variational model based on the TV norm [11] for super-resolution of multidimensional images. They use a new multi-scale approach (Bregman iterations) for iterative refinement and recovery of finer details in images. We will follow this approach to solve the more general super-resolution problem using the TV norm as regularizing functional. In addition, we propose an iterative refinement procedure based on an original idea by Bregman [1], to improve spatial resolution. The proposed super-resolution method improves upon the behavior of any interpolation method (including high order and sinc interpolation) because our method preserves edges satisfactorily avoiding Gibbs phenomenon, whereas the iterative refinement procedure allows us to recover fine scales of the image. The main contributions of this paper are as follows:

- a three-dimensional variational model based on the TV norm [11] regularizer.
- a new multi-scale approach (Bregman iterations) for iterative refinement and recovery of finer details in images.
- a new piecewise-linear up(down) sampling operator that preserves edges.
- application of this method for super-resolution for anisotropic 3D MRI images.

This paper is organized as follows: Section 2 outlines the super-resolution model using TV regularization. In particular, it explains the variational model as well as a new scale-space approach that utilizes the Bregman iterative procedure for recovering finer details from images. Additionally, section 2.2 proposes a new edge-preserving up (down) sampling operator used in the model. Section 3 presents details of the numerical implementation of the model. Section 4 demonstrates experimental results for a few 2D natural images as well as 2D slices and 3D volumes of MRI images, followed by the summary.

2 Image Observation and Synthesis Model

The low resolution image observation model can be formulated in a standard fashion as a down-sampled degraded version of the original high resolution image. We assume that the low resolution image f is defined on a subset of a plane $\Omega \subset \mathbb{R}^k$. For the purpose of this paper, k is either 2 or 3. Here onwards, all the notation will be specified for $3D$ images. The restriction to $2D$ images is straightforward. For a discrete representation, we assume $f \in \mathbb{R}^n \times \mathbb{R}^m \times \mathbb{R}^p$. Let the unknown high resolution image to be estimated be given by $u \in \mathbb{R}^{2m} \times \mathbb{R}^{2n} \times \mathbb{R}^{2p}$. Then given a linear down sampling operator D, we can write the observation model as,

$$f = D(h * u) + n, \tag{1}$$

where n is an additive Gaussian white noise with zero mean and variance σ^2, and h is a translation invariant convolution kernel corresponding to the point spread function of the imaging device. A related problem in the above formulation is the estimation of the kernel h, that we shall skip in this paper. Throughout this paper, we assume that the kernel is given by the Gaussian,

$$h(x, y, z) = K e^{-\frac{1}{2}\left[\frac{x^2}{\sigma_x^2} + \frac{y^2}{\sigma_y^2} + \frac{z^2}{\sigma_z^2}\right]}, \tag{2}$$

where K is a normalization constant, and $\sigma_x, \sigma_y, \sigma_z$ are variances along the X, Y, and Z directions respectively. The problem in Eqn. 1 is usually solved as a constrained optimization problem that seeks to minimize the regularizer $\int_\Omega ||\nabla u||^2 dxdy$, while constraining the noise to be $||h * u - f||_{\mathbb{L}^2}^2 = \sigma^2$. This ensures that the reconstructed image u is free of discontinuities. An alternative to the above regularizer is the total variation proposed by Rudin and Osher [11]. This norm is shown to recover edges in images satisfactorily. The total variation norm is given as,

$$\mathrm{TV}(u) = \int_{\Omega} |\nabla u| dxdy \tag{3}$$

Using the regularizer in Eqn. 3, we can state the single frame image reconstruction model as follows:

$$\hat{u} = \arg\min_{u} \{TV(u) + \frac{\lambda}{2}[||f - D(h * u)||^2_{\mathbb{L}^2} - \sigma^2]\} \tag{4}$$

The Euler-Lagrange formulation for Eqn. 4 can be written as

$$\nabla \cdot \frac{\nabla u}{|\nabla u|} + \lambda(\tilde{h} * S(f) - \tilde{h} * (S \circ D(h * u))) = 0 \tag{5}$$

$$\implies \nabla \cdot \frac{\nabla u}{|\nabla u|} + \lambda \tilde{h} * (\bar{g} - T(h * u)) = 0 \tag{6}$$

where S is an upsampling operator, $\tilde{h}$ is the inverse of h, $\bar{g} = S(f)$, and the operator T is defined as $T = S \circ D$. Furthermore $D \circ S = Id$

The Euler-Lagrange equation given by Eqn. 6 can be solved as a time-dependent equation

$$u_t = \nabla \cdot \frac{\nabla}{|\nabla u|} + \lambda \tilde{h} * (\bar{g} - T(h * u)) \tag{7}$$

with homogeneous Neumann boundary conditions and initiating with $u_0 = S(f)$.

2.1 Bregman Iterative Method

The convergence of Eqn. 7 to the steady state yields a reconstructed high resolution image. However if one wishes to recover even finer scales from the reconstructed image, one can use the Bregman iterative refinement procedure [1] to do so. If u_0 is the solution of Euler-Lagrange equation (6), then we have,

$$\nabla \cdot \frac{\nabla u_0}{|\nabla u_0|} + \lambda \tilde{h} * (\bar{g} - T(h * u_0)) = 0 \tag{8}$$

We will denote the image residual in the high resolution scale by v_0 as,

$$v_0 = \bar{g} - T(h * u_0) \tag{9}$$

We now solve the Euler-Lagrange equation for the new image $\bar{g} + v_0$ to obtain a new solution, which we denote by u_1. Again, the solution u_1 will satisfy

$$\nabla \cdot \frac{\nabla u_1}{|\nabla u_1|} + \lambda \tilde{h} * \Big(\bar{g} + v_0 - T(h * u_1)\Big) = 0, \tag{10}$$

where the new residual is defined as

$$v_1 = \bar{g} + v_0 - T(h * u_1) \tag{11}$$

and so on. The sequence of images $u_0, u_1, \cdots, u_j, \cdots$ are also referred to as Bregman iterates. It is advisable to terminate this procedure when a satisfactory image quality is obtained, otherwise it has a tendency to recover noise after all the finer scales in the image are recovered. This iterative procedure was introduced for image restoration in [10].

2.2 Edge-Preserving Up (Down)-Sampling Operator

There are various choices for the up (S) and down (D) sampling operators used in the observation model in Eqn. 1 and the synthesis model in Eqn. 7 respectively. The simplest down sampling operator can be an averaging operator that simply averages the eight neighbors of the pixel using either a Gaussian kernel, or an arithmetic average. Correspondingly, the up sampling operation simply involves repeating voxel values for each row, column, and slice. Alternately, one can also use bilinear interpolation for up sampling and down sampling images. The problems with the above approaches are the unnecessary blurring (averaging) that is caused at each step of the iteration while solving the Euler Lagrange equation in 6. To overcome this problem, one can use better signal preserving operators that involve sinc or Fourier interpolation for up and down sampling. However these methods can potentially introduce ringing artifacts in images with sharp edges or boundaries.

Especially for images with prominent edges and interfaces, we need an appropriate interpolation operator that preserves these features. Accordingly, we propose a new piecewise-linear up (down) sampling operator that preserves such edges and boundaries. We describe the edge-preserving operator in detail below. We set up the grid $x_j = (j-1)\Delta x, y_k = (k-1)\Delta y$ and $z_l = (l-1)\Delta z$, where $\Delta x > 0, \Delta y > 0, \Delta z > 0$ and $j = 1, \ldots, n, k = 1, \ldots, m$ and $l = 1, \ldots, p$. We define the domain $E = [0, A] \times [0, B] \times [0, C]$, where $A = (n-1)\Delta x$, $B = (n-1)\Delta y$, and $C = (n-1)\Delta z$. We consider the grid function u defined as

$$u_{j,k,l} : \mathbb{R}^3 \to \mathbb{R}$$

We define the **edge-preserving piecewise linear approximation** of the grid function u as the function $L(x, y, z)|_{E_{jkl}} = L_{jkl}(x, y, z)$ where the computational voxel E_{jkl} is given by

$$E_{jkl} = [x_j - \frac{\Delta x}{2}, x_j + \frac{\Delta x}{2}] \times [y_k - \frac{\Delta y}{2}, y_k + \frac{\Delta y}{2}] \times [z_l - \frac{\Delta z}{2}, z_l + \frac{\Delta z}{2}]$$

and

$$L_{jkl}(x, y, z) = u_{j,k,l} + a(x - x_j) + b(y - y_k) + c(z - z_l),$$

where a, b, and c are determined from $a = \text{minmod}\left(\frac{\Delta^x_- u_{j,k,l}}{\Delta x}, \frac{\Delta^x_+ u_{j,k,l}}{\Delta x}\right)$, $b = \text{minmod}\left(\frac{\Delta^y_- u_{j,k,l}}{\Delta y}, \frac{\Delta^y_+ u_{j,k,l}}{\Delta y}\right)$, and $c = \text{minmod}\left(\frac{\Delta^z_- u_{j,k,l}}{\Delta z}, \frac{\Delta^z_+ u_{j,k,l}}{\Delta z}\right)$, where the operations in the term containing derivatives are understood component-wise, and given by $\Delta^x_\pm u^n_{i,j,k} = \pm(u^n_{i\pm1,j,k} - u^n_{i,j,k})$, $\Delta^y_\pm u^n_{i,j,k} = \pm(u^n_{i,j\pm1,k} - u^n_{i,j,k})$, and $\Delta^z_\pm u^n_{i,j,k} = \pm(u^n_{i,j,k\pm1} - u^n_{i,j,k})$, where i, j, k are the indices of the 3D grid.

The minmod(d, e) function is defined as,

$$\text{minmod}(d, e) = \frac{\text{sgn}(d) + \text{sgn}(e)}{2} \min(|d|, |e|), \tag{12}$$

where sgn$(d) = 1$ if $d \geq 0$ and sgn$(d) = -1$ otherwise.

The function $L_{jkl}(x, y, z)$ is defined on the computational voxel E_{jkl}. We want to up-(down) sample the grid function u with a spatial resolution of $h_x > 0, h_y > 0, h_z > 0$. Then the up-(down) sampled grid function v is defined on a new grid $v(q, r, s)$ for $q = q, \ldots, nh, r = 1, \ldots, mh$, and $s = 1 \ldots, ph$ where

$$nh = \text{floor}\left(\frac{A}{h_x}\right), mh = \text{floor}\left(\frac{B}{h_y}\right), ph = \text{floor}\left(\frac{C}{h_z}\right),$$

where floor(d) is the maximum of all integers i such that $i \leq d$. The new grid is then defined as $x_{h_q} = (q-1)h_x, y_{h_r} = (r-1)h_y$, and $z_{h_s} = (s-1)h_z$. Based on this grid, the function v is defined as $v(q, r, s) = L(x_{h_q}, y_{h_r}, z_{h_s})$.

We demonstrate the edge-preserving property of the above operator by applying it to a checkerboard pattern as shown in Fig. 1. Figure 1 shows a low-resolution image, as well as its up sampled versions using a bilinear, sinc and the edge-preserving operator for two different types of checkerboard patterns. It also shows a magnified portion from the center of the image. It is observed that the bilinear and the sinc interpolation operators introduce significant spurious levels of gray in between the black squares in the pattern. Furthermore, they have a tendency to smooth out the boundaries of the flat black squares in the image. In contrast, the edge-preserving operator has retained, and in some cases even enhanced the boundaries and edges as compared to the low-resolution image.

Figure 3 shows similar results with a 280 × 200 scene image. The first image in the top row shows the 560×400 pixel replicated image, whereas the last image is the super-resolved image. The bottom row shows a small portion of the image magnified to show detail. One can immediately observe the blocking effects due to pixel replication in the first image, and blurring of the edge boundaries in the bilinearly interpolated version. The edges get somewhat better using the sinc interpolation, but the best quality is given by the super-resolved image, that resolves and even enhances sharp edges and interfaces in the image. In both the above cases, we used an isotropic Gaussian kernel with kernel widths $\sigma_x = \sigma_y = 1$.

3 Numerical Implementation

This section discusses the numerical implementations of the solution to the Euler Lagrange equation. The Euler-Lagrange derivative of the TV-norm is not well defined at points where $\nabla u = 0$, due to the presence of the term $\frac{1}{|\nabla u|}$. Hence we modify the regularization TV functional as follows:

$$\int_{\Omega} \sqrt{|\nabla u|^2 + \epsilon} \, dxdy \tag{13}$$

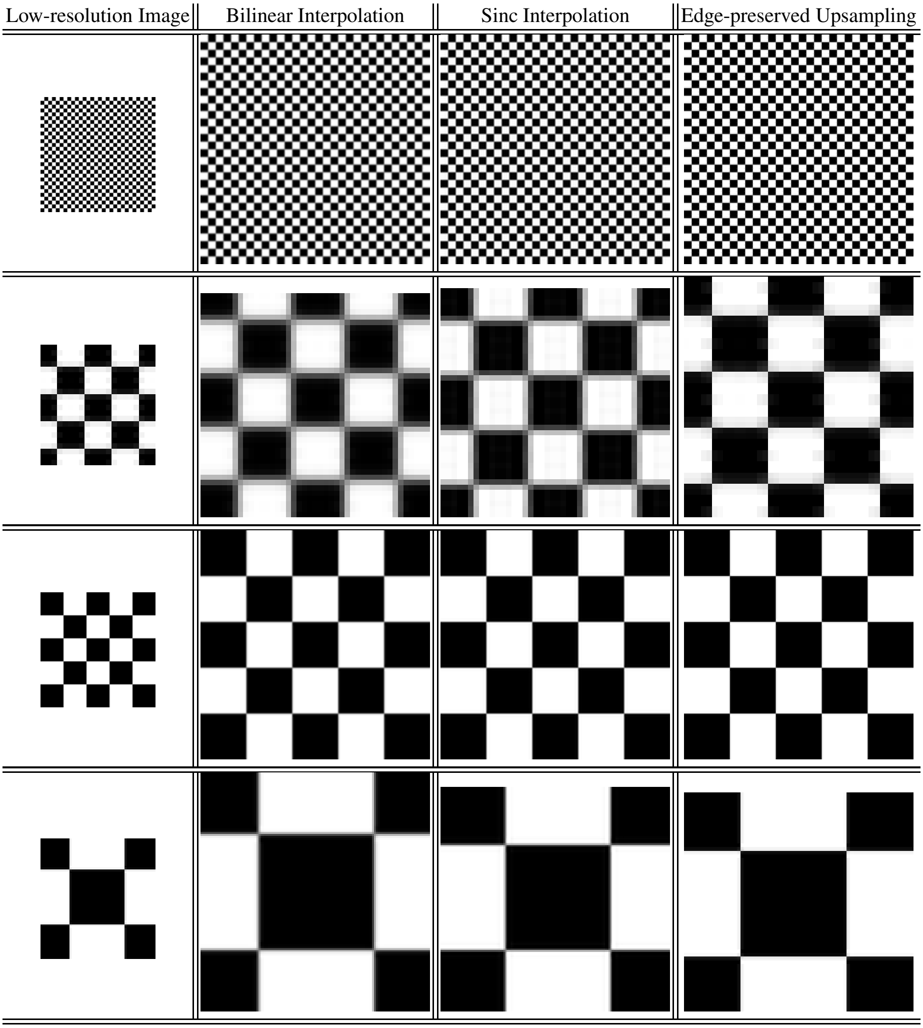

Fig. 1. The first and the third rows show a low-resolution image from the left, and its up sampled versions using a bilinear interpolation operator, a sinc operator, and the new edge-preserving operator for two different checkerboard patterns. The second and the fourth rows show a magnified area from the center of the image.

where ϵ is a small positive parameter. We express the 3D model (7) in terms of explicit partial derivatives

$$\begin{aligned} u_t =& \lambda \tilde{h} * (\bar{g} - T(h * u)) \\ &+ \frac{u^n_{xx}((u^n_y)^2 + (u^n_z)^2 + \epsilon)) + u^n_{yy}((u^n_x)^2 + (u^n_z)^2 + \epsilon)) + u^n_{zz}((u^n_x)^2 + (u^n_y)^2 + \epsilon))}{[(u^n_x)^2 + (u^n_y)^2 + (u^n_z)^2 + \epsilon]^{3/2}} \\ &+ \frac{-2u^n_{xy}u^n_x u^n_y - 2u^n_{xz}u^n_x u^n_z - 2u^n_{yz}u^n_y u^n_z}{[(u^n_x)^2 + (u^n_y)^2 + (u^n_z)^2 + \epsilon]^{3/2}} \end{aligned} \tag{14}$$

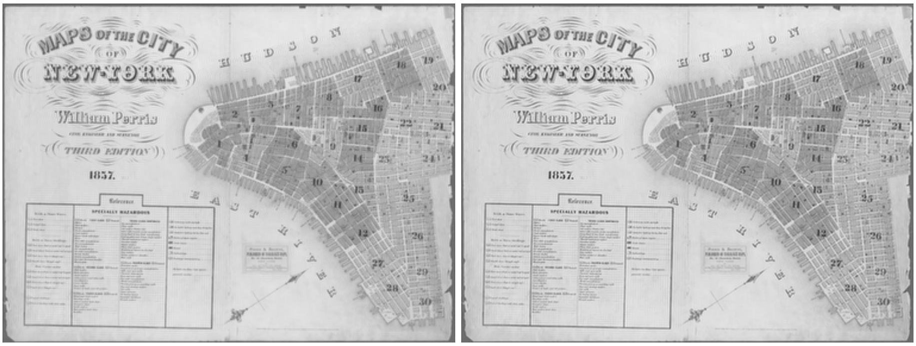

low-resolution image sinc interpolation

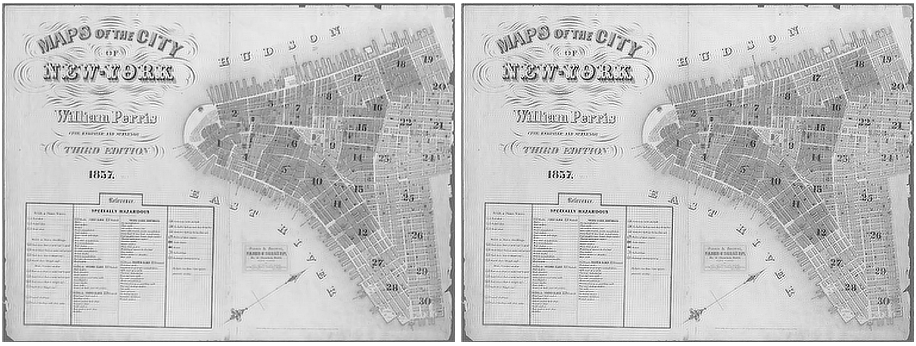

Super-resolved reconstruction 1^{st} Bregman refinement

Fig. 2. Clockwise from top, a 380×285 low-resolution image, upsampled to twice the size by sinc interpolation, and super-resolved reconstruction, and the first Bregman iterated image

using $u_0 = S(f)$ as the initial guess and homogeneous Neumann boundary conditions (i.e. absorbing boundary).

The above expression can also be rewritten as

$$\frac{u^{n+1}_{i,j,k} - u^n_{i,j,k}}{\Delta t} = \lambda[\tilde{h} * (\bar{g} - T(h * u^n))]_{i,j,k} \tag{15}$$

$$+\frac{u^n_{xx}((u^n_y)^2+(u^n_z)^2+\epsilon))+u^n_{yy}((u^n_x)^2+(u^n_z)^2+\epsilon))+u^n_{zz}((u^n_x)^2+(u^n_y)^2+\epsilon))}{[(u^n_x)^2+(u^n_y)^2+(u^n_z)^2+\epsilon]^{3/2}} \tag{16}$$

$$+\frac{-2u^n_{xy}u^n_x u^n_y - 2u^n_{xz}u^n_x u^n_z - 2u^n_{yz}u^n_y u^n_z}{[(u^n_x)^2 + (u^n_y)^2 + (u^n_z)^2 + \epsilon]^{3/2}} \tag{17}$$

The approximations to the derivatives in Eqn. 17 can be calculated as: $[u^n_{xx}]_{i,j,k} = \Delta^x_+ \Delta^x_- u^n_{i,j,k}/h^2_x$, $[u^n_{yy}]_{i,j,k} = \Delta^y_+ \Delta^y_- u^n_{i,j,k}/h^2_y$, $[u^n_{zz}]_{i,j,k} = \Delta^z_+ \Delta^z_- u^n_{i,j,k}/h^2_z$, $[u^n_{xy}]_{i,j,k} = (\Delta^x_- + \Delta^x_+)(\Delta^y_- + \Delta^y_+)u^n_{i,j,k}/4(h_x h_y)$, $[u^n_{xz}]_{i,j,k} = (\Delta^x_- + \Delta^x_+)(\Delta^z_- + \Delta^z_+)u^n_{i,j,k}/4(h_x h_z)$, $[u^n_{yz}]_{i,j,k} = (\Delta^y_- + \Delta^y_+)(\Delta^z_- + \Delta^z_+)u^n_{i,j,k}/4(h_y h_z)$, $[u^n_x]_{i,j,k} = (\Delta^x_- + \Delta^x_+)u^n_{i,j,k}/2h_x$, $[u^n_y]_{i,j,k} = (\Delta^y_- + \Delta^y_+)u^n_{i,j,k}/2h_y$, $[u^n_z]_{i,j,k} = (\Delta^z_- + \Delta^z_+)$

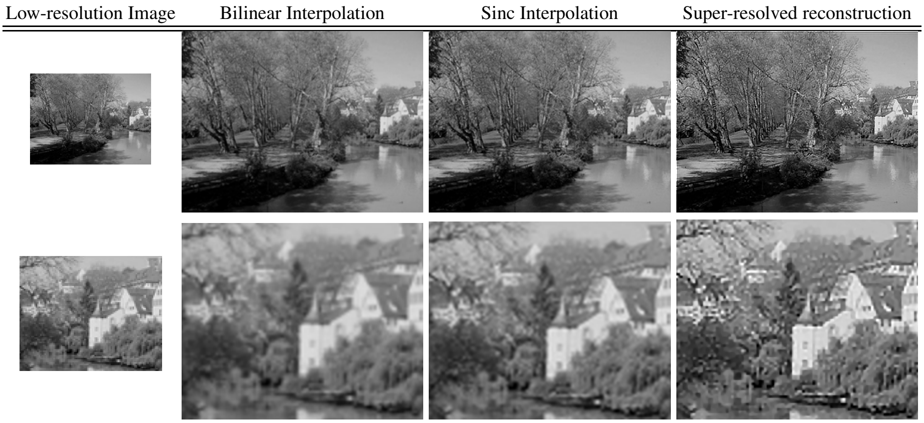

Fig. 3. Top row shows the low-resolution image, and the upsampled versions using bilinear, sinc and the super-resolved reconstruction. The bottom row shows a magnified detail of a portion of the image.

$u^n_{i,j,k}/2h_z$ The Lagrange multiplier λ was chosen to be the maximum value for which the algorithm was stable. It was empirically determined to be $\lambda = 10$, and was not changed thereafter.

4 Experimental Results

Lastly, we demonstrate the algorithm by performing experiments with 2D natural images, 2D slices of 3D volumetric images, and finally the full 3D volumetric MRI images themselves.

4.1 Results for Natural Images

Figure 2 shows the results of the super-resolution reconstruction algorithm applied to a 380×285 map image. This image has been scaled to 760×570 by pixel-replication for display purposes. It can be observed that pixel replication inherently adds blocking artifacts to the image. The low-resolution image is up sampled by a factor of two using bilinear interpolation, and sinc interpolation, and finally using the super-resolution reconstruction method. It is observed that bilinear interpolation grossly smoothes out the image, the result due to sinc interpolation is preserves some high frequency information, whereas the super-resolved reconstruction yields a sharp, crisp image, even resolving the little text at finer scales. One can further enhance this image by performing the 1^{st} Bregman iteration as shown in Fig. 2. However, this process should be terminated after one or two iterations.

4.2 Results for 2D Slices of 3D MRI Image

In this experiment, we look at enhancing the in-plane resolution of individual transverse slices of a 3D MRI image. From left, all rows of Fig. 4 show an isotropic original image

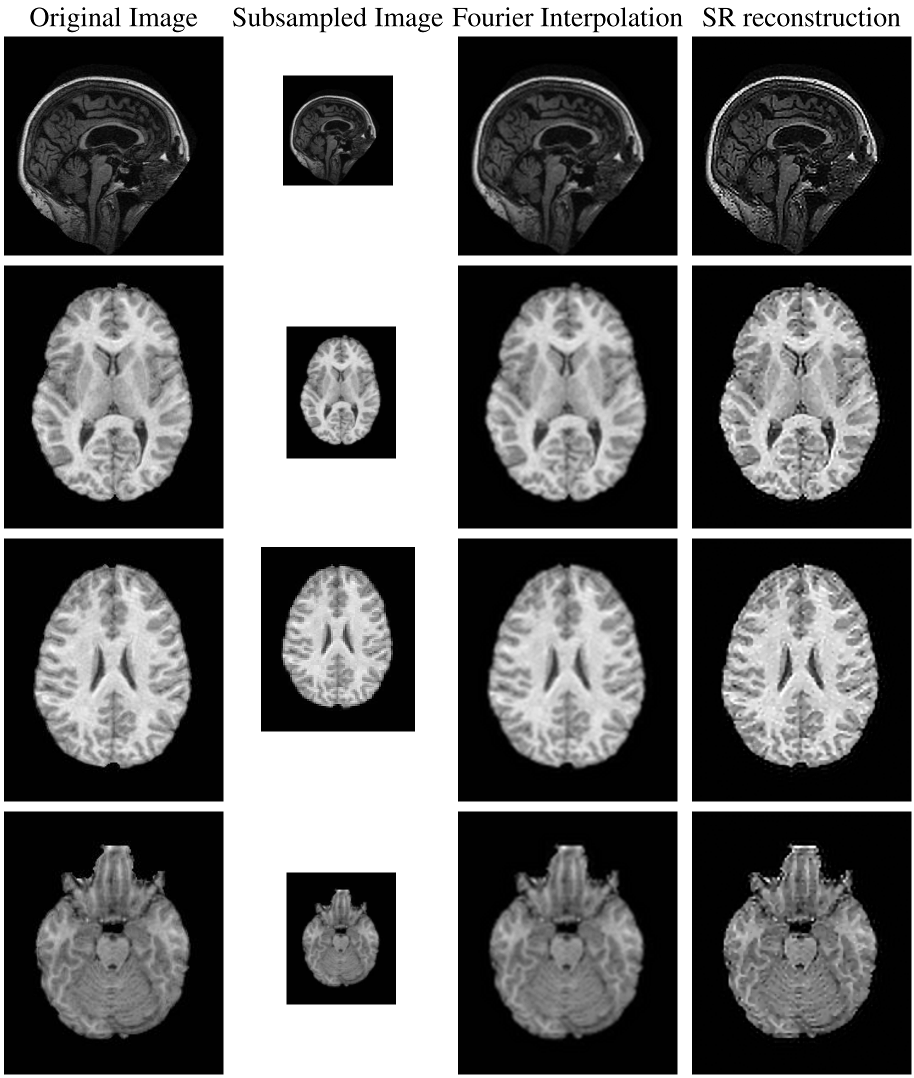

Fig. 4. Examples of super-resolved reconstruction for 2D slices of 3D MRI images

180×216, the subsampled image, a Fourier interpolated image, and a super-resolved reconstructed image. For display purposes, the subsampled image is shown at twice the resolution using pixel-replication. It is observed that the high resolved reconstructed image has sharper edge features, more details, and visually closely resembles the original image as compared to the Fourier interpolated result.

4.3 Results for Full 3D MRI Images

The proposed super-resolution algorithm can be applied to arbitrary 2D images or even 3D volumes of anisotropic voxel dimensions. In this experiment, we apply the reconstruction

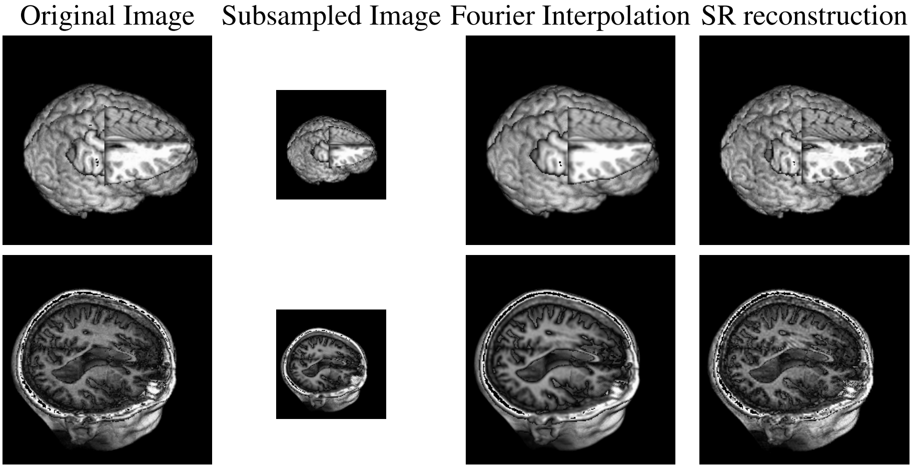

Fig. 5. Examples of super-resolved reconstruction for full 3D MRI images (volume rendered)

algorithm to the full 3D MRI image volume. Figure 5 shows a volume rendering of an original image of dimensions $256 \times 256 \times 160$, at voxel widths given by $1 \times 1 \times 1.25\, mm^3$. This image is first subsampled to half the resolution at $128 \times 128 \times 80\, (2 \times 2 \times 2.5\, mm^3)$ and then super-resolved to a full isotropic $256 \times 256 \times 160$ image with $1 \times 1 \times 1\, mm^3$ resolution. As expected, we can see an improvement in the resolution plus an increase in the detail simultaneously across all X, Y, and Z dimensions. In this experiment, we used an anisotropic Gaussian kernel with the variances proportional to the voxel dimensions. Furthermore the grid dimensions for the edge-preserving up sampling and down sampling operators were taken to be $\Delta x = \frac{h_x}{2}$, $\Delta y = \frac{h_y}{2}$, $\Delta z = \frac{h_z}{2}$, where h_x, h_y, h_z are the voxel dimensions of the appropriate up sampled or down sampled image.

5 Conclusion and Future Directions

We have presented a method for enhancement of resolution of images. The strengths of this approach lie in the i) TV norm as a regularizing functional in the variational model, and ii) a new piecewise-linear up(down) sampling operator that preserves edges. While we are aware that the proposed method works with the physical space, and not the frequency (k-space) of the data, we emphasize that the TV prior is a nonlinear prior that does modify the amplitudes of the k-space data. In other words, our algorithm works on the processed physical image, yet it modifies the spectral information implicitly in the data. This is an important point to be noted, especially in view of comparison with other methods that involve MRI image processing that work with the k-space representation of the data. We have demonstrated the improvement in spatial resolution for 2D as well as 3D anatomical MRI images. In the future, we intend to investigate the problem of high resolution reconstruction of DT-MRI images using the proposed method.

Acknowledgments

This research was partially supported by the National Institute of Health through the NIH Roadmap for Medical Research, Grant U54 RR021813. Additionally, Dr. Antonio Marquina gratefully acknowledges the support from the NSF grants DMS-0312222, ACI-0321917, the NIH grant G54 RR021813, as well as DGICYT MTM2008-03597 from the Spanish Government Agency.

References

1. Bregman, L.M.: The relaxation method of finding the common point of convex sets and its application to the solution of problems in convex programming. USSR Comput. Math. and Math. Phys. 7, 200–217 (1967)
2. Capel, D., Zisserman, A.: Super-resolution from multiple views using learnt image models. In: CVPR, vol. 2, pp. 627–634 (2001)
3. Carmi, E., Liu, S., Alon, N., Fiat, A., Fiat, D.: Resolution enhancement in MRI. Magnetic Resonance Imaging 24(2), 133–154 (2006)
4. Chaudhuri, S., Joshi, M.: Motion-Free Super-Resolution. Springer, New York (2005)
5. Elad, M., Feuer, A.: Restoration of a single super-resolution image from several blurred,noisy, and undersampled measured images. IEEE Tran. Image Processing 6(12), 1646–1658 (1997)
6. Freeman, W.T., Jones, T.R., Pasztor, E.C.: Example-based super-resolution. IEEE Computer Graphics and Applications 22(2), 56–65 (2002)
7. Greenspan, H., Oz, G., Kiryati, N., Peled, S.: MRI inter-slice reconstruction. Magnetic Resonance Imaging 20, 437–446 (2002)
8. Irani, M., Peleg, S.: Improving resolution by image registration. CVGIP: Graphical Models and Image Processing 53(3), 231–239 (1991)
9. Kornprobst, P., Peeters, R., Nikolova, M., Deriche, R., Ng, M., Van Hecke, P.: A superresolution framework for fMRI sequences and its impact on resulting activation maps. In: Ellis, R.E., Peters, T.M. (eds.) MICCAI 2003. LNCS, vol. 2879, pp. 117–125. Springer, Heidelberg (2003)
10. Osher, S.J., Burger, M., Goldfarb, D., Xu, J., Yin, W.: An iterative regularization method for Total Variation-based image restoration. Multiscale Modeling and Simulation 4(2), 460–489 (2005)
11. Rudin, L.I., Osher, S.J., Fatemi, E.: Nonlinear Total Variation based noise removal algorithms. Physica D 60(1-4), 259–268 (1992)
12. Startk, H., Oskoui, P.: High-resolution image recovery from image-plane arrays, using convex projections. Journal of the Optical Society of America 6, 1715–1726 (1989)
13. Tsai, R.Y., Huang, T.S.: Multi-frame image restoration and registration. In: Advances in Computer Vision and Image Processing, pp. 317–339 (1984)
14. Marquina, A., Osher, S.J.: Image super-resolution by TV-regularization and Bregman iteration. Journal of Scientific Computing 37(3), 367–382 (2008)